JGR

Key Points:
- Energetic neutral atom imaging can be done without filtering ambient ultraviolet light
- Angular resolution of 2° and energy range to below 1 keV for hydrogen can be achieved at higher sensitivity than previously
- Background rejection sufficient to operate in Jupiter's magnetosphere in the vicinity of Ganymede is possible

Correspondence to:
D. G. Mitchell,
Donald.G.Mitchell@jhuapl.edu

Energetic particle imaging: The evolution of techniques in imaging high-energy neutral atom emissions

D. G. Mitchell[1], P. C. Brandt[1], J. H. Westlake[1], S. E. Jaskulek[1], G. B. Andrews[1], and K. S. Nelson[1]

[1]Johns Hopkins University Applied Physics Laboratory, Laurel, Maryland, USA

Abstract Energetic neutral atom imaging instruments have been flown on a variety of space missions to satisfy a variety of science requirements. In this paper we discuss the most recent developments that lead to improvements in energy range, angular resolution, and background rejection for the high-energy range, as represented in the past by the Cassini magnetosphere imaging instrument Ion and Neutral Camera, the Imager for Magnetopause-to-Aurora Global Exploration (IMAGE) mission High-Energy Neutral Atom instrument, and to some degree the IMAGE mission Medium-Energy Neutral Atom instrument. The new approaches discussed here rely on the use of ultrathin foils without UV filters and on very high speed coincidence logic to reduce accidentals from intense background sources. We present laboratory results demonstrating an electrostatic design that meets the coincidence timing requirements, position, and scattering performance consistent with angular resolution (full width at half maximum) of ~2° for hydrogen above 10 keV and a hydrogen energy threshold ≤1 keV.

1. Introduction

Energetic neutral atoms (ENAs) are produced in magnetized space plasmas when energetic singly ionized ions (H^+, O^+, etc.) undergo charge exchange with an ambient neutral gas atom. The energetic ion acquires an electron from the (typically cold) gas atom, leaving behind a cold ionized gas atom. Now neutral, the ENA is no longer influenced by the magnetic field and radiates away from the hot plasma, where it originated along a nearly straight trajectory (gravity being a negligible effect in most cases). By measuring the velocity and species of the emitted neutrals with an appropriate instrument, information about the source plasma can be inferred. With an instrument designed to image the emission of ENAs (effectively an ENA camera), a series of images can be produced for a range of species and energies as a function of time, allowing the spatial, temporal, and plasma characteristics of a hot plasma population (magnetospheric, ionospheric, and heliospheric) to be determined. See *Williams et al.* [1992] and *Gruntman* [1997] for the comprehensive reviews of this technique.

Imaging of ENAs has played an important role in several NASA missions, most notably the Imager for Magnetopause-to-Aurora Global Exploration (IMAGE) mission [*Burch*, 2000], the Cassini mission (joint with European Space Agency (ESA)), and the Interstellar Boundary Explorer (IBEX) mission [*McComas et al.*, 2009a]. In this paper we will focus on advances to the basic design of IMAGE High-Energy Neutral Atom (HENA) imager [*Mitchell et al.*, 2000] and Cassini Magnetospheric Imaging Instrument Ion and Neutral Camera (INCA) [*Krimigis et al.*, 2004] for application to instruments for future missions. The development effort has included both Johns Hopkins University Applied Physics Laboratory (APL) internal Independent Research and Development and NASA instrument development support, and now we are refining and developing specific features to meet the requirements of the NASA-supported Jovian Energetic Neutrals and Ions (JENI) instrument to be flown on the ESA Jupiter Icy Moons Explorer (JUICE) mission to Jupiter, Ganymede, and Europa. These features are not unique to the JUICE application but rather are quite general advances applicable to a variety of missions for which high-energy neutral atom imaging is implemented.

While a variety of approaches to imaging ENAs have been proposed, and several developed and flown, the most common involve (1) impact of the ENA on a surface where it is reionized and subsequently analyzed using techniques for detecting charged particles. This approach is best suited to very low energy neutrals and (2) the transit of the ENA through a very thin foil before impacting an imaging back-plane detector a prescribed distance from that foil. Secondary electrons emitted from the thin foil are electrostatically deflected into a start detector placed out of the ENA flight path, where the time and position of the foil transit are recorded. The ENA impact with the back-plane (stop) detector generates a stop time and position, which

together with the start time and position provide the ENA velocity (speed and direction). For some combinations of ENA energy and stop detector characteristics, the ENA energy may also be determined, yielding the ENA mass in addition to its velocity. Again, see *Gruntman* [1997] for a review of a variety of approaches to this measurement.

One hybrid approach has been used quite effectively, in the case of the Interstellar Boundary Explorer High Energy (IBEX-Hi) instrument on the IBEX mission. For this instrument, the ENAs penetrate a very thin foil in the entrance, after which the fraction of the ENAs that have been ionized during the interaction with the foil are electrostatically analyzed and postaccelerated through a time-of-flight (TOF) chamber. Although the fraction of the incident ENA that exits the front foil positively charged is quite low (10% to <1% over the sensor energy range), the electrostatic analyzer suppresses backgrounds from UV light by many orders of magnitude allowing a high signal-to-noise ratio to be achieved.

This paper will focus on improvements to the techniques used in the second of the two general approaches outlined above. Whereas the approach described seems straight forward, there are practical limitations to its implementation that compromise the quality of the ENA images produced. The detectors typically employed in the instruments that have been developed and flown are microchannel plate (MCP) detectors, composed of either a chevron configuration (two MCPs) or a Z-stack (three MCPs) backed up by a high time resolution imaging anode. The MCP stack typically multiplies the signal produced by the impact of a single electron by 6 to 7 orders of magnitude. These detectors are very sensitive to impacting electrons and/or ions but also respond to penetrating particles (e.g., radiation belt electrons and cosmic rays) as well as far ultraviolet (FUV) and extreme ultraviolet (EUV) light, with efficiencies ranging between ~30%, ~1%, and ~10%, respectively. These sources of background can be mitigated in a variety of ways. For penetrating particles, shielding can limit the fluxes to very high energies and so cut down on the event rates. For ultraviolet light, transmission filtering by various techniques can greatly reduce the intensity seen by the detectors. In each case (penetrators and UV) the goal is to reduce the rates on the individual detectors sufficiently that the rate of false start-stop coincidences (known as "accidentals") masquerading as real start-stop TOF events is low compared with the valid ENA-driven TOF events.

The two primary implementations of foil transmission-type ENA imagers flown to date are the above-mentioned INCA (and HENA), which used entrance foils designed as filters to reduce the UV intensities to acceptable levels, and the Medium-Energy Neutral Atom (MENA; IMAGE and Two Wide-angle Imaging Neutral atom Spectrometers (TWINS)) that used transmission gratings that attenuates the UV, again sufficiently to reduce the accidental rates to acceptable levels. Each has its strengths and drawbacks. In the case of INCA and HENA, the thickness of the start foil required to attenuate the UV limited the energy range to hydrogen above ~10 to 20 keV, and oxygen above ~30 to 50 keV, and resulted in significant angular scattering of the ENAs such that the image resolution at the lower energies was well below the ~3° resolution that the detector optics would otherwise have supported. In the case of MENA, the transmission gratings reduced the particle transmission by about a factor of 10, a direct hit to sensitivity. Since ENA intensities are typically very weak, such penalties directly affect counting statistics and so time resolution and signal-to-noise ratio.

The primary new developments discussed in this work are aimed at modifying the approach taken with INCA and HENA to achieve higher image angular resolution, reduce the minimum ENA energy to that achieved with MENA while maintaining sensitivity characteristic of INCA, and improve signal-to-noise ratio. The changes required for high angular resolution involve reducing the entrance start foil thickness from 10 to 15 $\mu g/cm^2$ used in INCA and HENA to a thickness of ~1–2 $\mu g/cm^2$. This allows improvement of angular resolution from ~6° for INCA and HENA to ~2° FWHM over much of the energy range. It also allows extension of the technique to a lower-energy bound of ≤1 keV for hydrogen as compared to ~10 keV for HENA and INCA. Additionally, new coincidence techniques permit the new design to achieve a useful signal-to-noise ratio (SNR) even in the high penetrating background radiation environment in Jupiter's magnetosphere. These same techniques also allow us to image ENA while largely eliminating backgrounds from UV light without relying on the entrance foils as UV filters and also without requiring specific UV filters such as those used by the IMAGE MENA instrument [*Pollock et al.*, 2000] and the similar TWINS instruments [*McComas et al.*, 2009b]. The design also can incorporate a line of pixels of solid state detectors (SSDs) over a strip in its back plane, providing well-discriminated ion and ENA composition for particle energies above the SSD threshold. This feature is included in the JENI design.
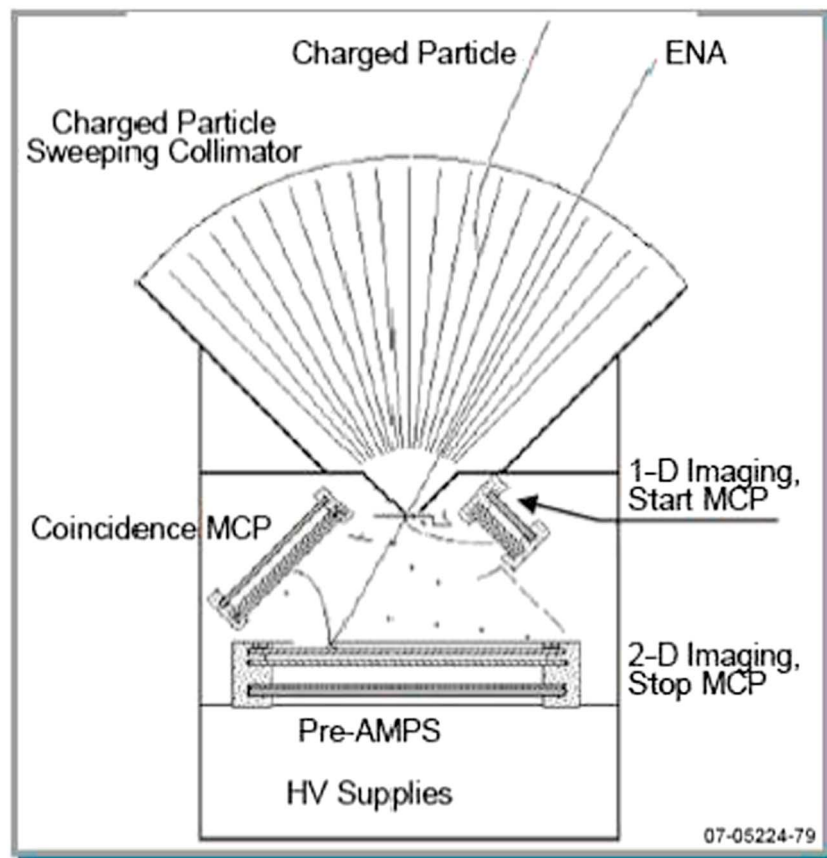
Figure 1. Schematic cross section of INCA. Charged particles are rejected by the electric fields in the collimator. ENAs traverse the collimator into the instrument where their TOF is measured. INCA also had a coincidence microchannel plate to further discriminate against uncorrelated start-stop coincidences (accidentals). We used this feature in INCA valid event logic during Earth flyby, and it has been enhanced in the JENI design with a tighter timing window and position correspondence with the stop position.

Although originally conceived as ENA imagers, these same instruments make excellent ion instruments as well (as with Ion and Neutral Camera (INCA)). With the voltage on the charged particle rejection plates in the entrance collimator set to zero, the high angular resolution provides detailed pitch angle distributions of energetic ions, with species discrimination above the SSD thresholds. Furthermore, energetic electrons can also be measured using the SSDs, though with less angular resolution. Since ion and ENA intensities generally differ by a few orders of magnitude, JENI has a variable aperture mechanism that is used to reduce the effective area of the entrance slit when high particle intensities might otherwise drive the sensor above the counting rate levels for which its response can be calibrated (whether throughput limitations of the electronics or direct saturation of the MCP detectors themselves), a critical component for the Jovian environment but optional in other possible applications.

2. Present State of ENA Imaging Designs: INCA Instrument

The INCA sensor (Figures 1 and 2) was completed 20 years ago. INCA was launched in October 1997 and has been returning images continuously since arrival at Saturn in July 2004 (and almost continuously since the Jupiter encounter in late 2000). The INCA instrument was crucial to understanding the global structure and dynamics of the Saturnian magnetosphere [e.g. *Krimigis et al.*, 2005; *Mitchell et al.*, 2005a], the interaction of Saturn's magnetosphere with Titan's atmosphere [e.g., *Mitchell et al.*, 2005b; *Brandt et al.*, 2012], and has also provided a unique vantage point and energy range for imaging the heliosphere in ENAs [*Krimigis et al.*, 2009; *Dialynas et al.*, 2013].
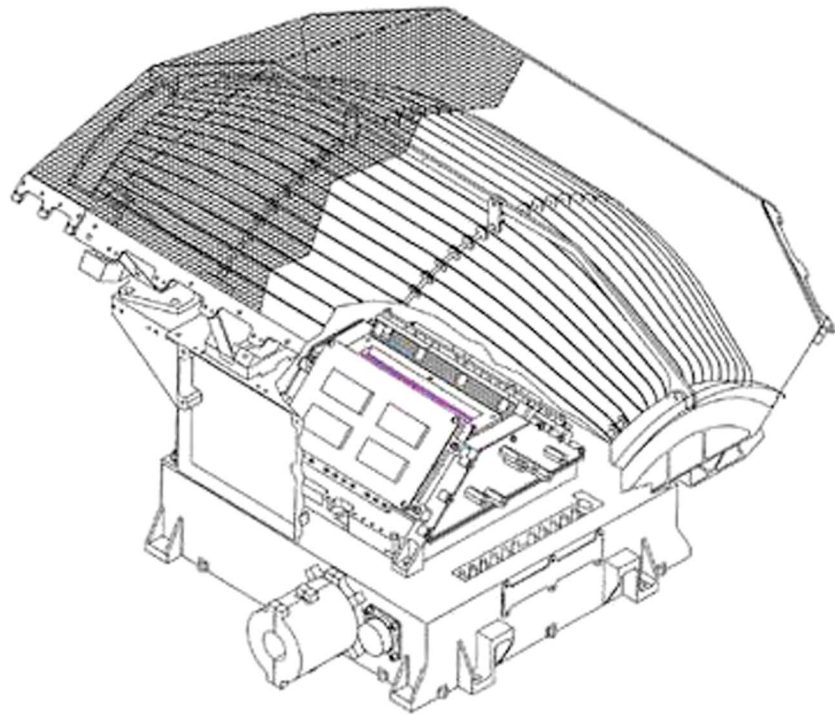
Figure 2. INCA cutaway—the entrance slit is highlighted in violet.

INCA would fit inside an envelope of $28 \times \sim 30 \times \sim 40$ cm), it weighs 7 kg, and it dissipates 3 W. It has a field of view of $90° \times \sim 120°$. INCA measures hydrogen ENAs between ~7 and 200 keV and oxygen ENAs between ~32 and 200 keV. INCA uses pinhole optics to form images of ENA emission regions.

Particles entering the sensor pass through a strong electric field between the alternately biased high-voltage plates in the collimator (Figure 1). The electric field sweeps charged particles into the plate surfaces, which are serrated to inhibit forward scattering. Below the ion energy per charge that can pass through them without impacting their surfaces, these plates have been shown (in flight and in the lab) to reduce the incident ion flux by more than 4 orders of magnitude.

ENAs continue in a straight line and enter the detector region through a thin foil in the entrance slit. As they pass through this foil, the ENAs generate secondary electrons. A shaped electric field within the detector region accelerates and guides the secondary electrons into a start detector, the MCP-based detector where a timing pulse is recorded to measure the ENA's time of flight (TOF) through the sensor. In addition, the start detector also measures the position in the dimension out of the plane of the figure. The ENA continues to the back plane, where it passes through another thin foil and strikes the stop MCP-based detector. The stop detector records the stop time for the TOF measurement and the impact position in both dimensions. Together, the two positions determine the ENA trajectory, while the TOF determines its speed. Images are accumulated over time, as the ENA events are binned according to their velocity and direction of arrival. Valid event logic can be commanded to require or ignore the coincidence pulse (recorded by a third MCP-based detector, from secondary electrons backscattered off the stop foil). During Cassini's Earth flyby, the coincidence signal was required for valid events. However, this feature has not been used on INCA since, as sufficient signal/noise (S/N) was achieved without it and employing it reduces the sensor efficiency by about a factor of 3 for hydrogen and/or protons (the distinction is not important to any of the sensor elements beyond the deflection plates, since the initial charge state of the particle (ion or ENA) is lost as it transits the start foil).

3. The JENI Sensor

The JENI instrument is part of the Particle Environment Package on the JUICE mission. JENI (Figure 3) incorporates high time and position resolution MCP measurements to both image and measure the velocity of particles (ENA or ions) that enter either of the two, 8 cm long slit apertures.
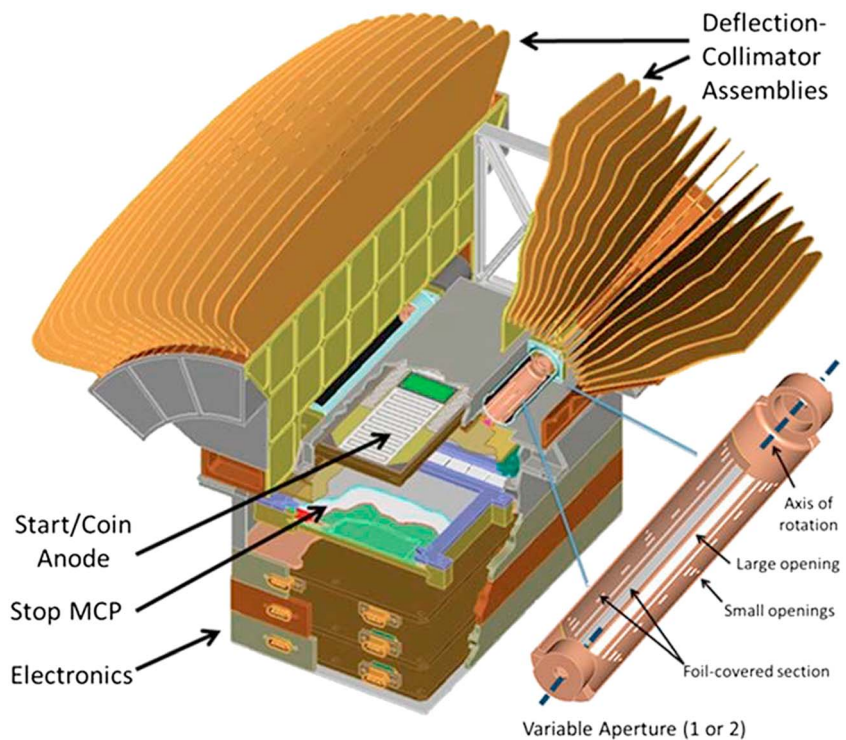
Figure 3. JENI CAD drawing showing major elements: collimator plates (with serrated surfaces and biased with alternating ground and positive high voltage), start/coincidence MCP assembly with two 1-D start anodes servicing two entrance slits and one 1-D coincidence anode down the center, variable aperture rotating cylinder mechanisms servicing each entrance slit (highlighted, right), two stop MCPs backed up by 2-D anodes, and a strip of SSD pixels between the two stop MCPs providing high-resolution particle composition capability.

3.1. Deflection and Collimator Assemblies

When they are energized with high voltage, a set of thin, conductive plates (serrated on both sides to inhibit forward scattering of particles) sweep ions and electrons out of the trajectories that can enter the slit entrances on either side of the sensor. This is a minor reconfiguration of the same subsystem used very effectively on the Cassini INCA sensor and the IMAGE HENA sensor. The JENI implementation has slightly larger gaps between the plates, and can be run up to 8 kV potential drops, excluding charged particles up to ~300 keV/q.

3.2. Variable Aperture

By rotating a cylindrical section populated with a variety of apertures (Figure 3), a stepper motor controls the pattern of the aperture slit to one of a variety of configurations accommodating different geometric factors, as well as allowing for UV filtering when the Sun is in the FOV. The variable aperture mechanism on each slit can be controlled independently, so that for example the sunlight filter can be used on one aperture and not on the other, as needed.

3.3. Start Assembly

After passing through the entrance slit, a particle penetrates the start foil (Figure 4), producing secondary electrons at the exit surface of the foil. This is an ~1 $\mu g/cm^2$ grid-supported carbon foil that runs the length of the entrance slit. Internal grids shape the electric field to accelerate and reflect the secondary electrons (green traces) into the start region of the start-coincidence detector, which serves both start and coincidence timing and position functions. The 1-D positioning start anodes back this MCP detector on either side, with a 1-D positioning coincidence anode backing the middle (Figure 5). The start anodes return pulses from either end of a time delay trace (~40 ns total delay). The measured time difference between the two pulses identifies the position to ~1 mm of the MCP output pulse in the dimension out of the plane of Figure 4. The entrance slit width constrains the position in the other dimension for the start. The TOF start time is derived by correcting
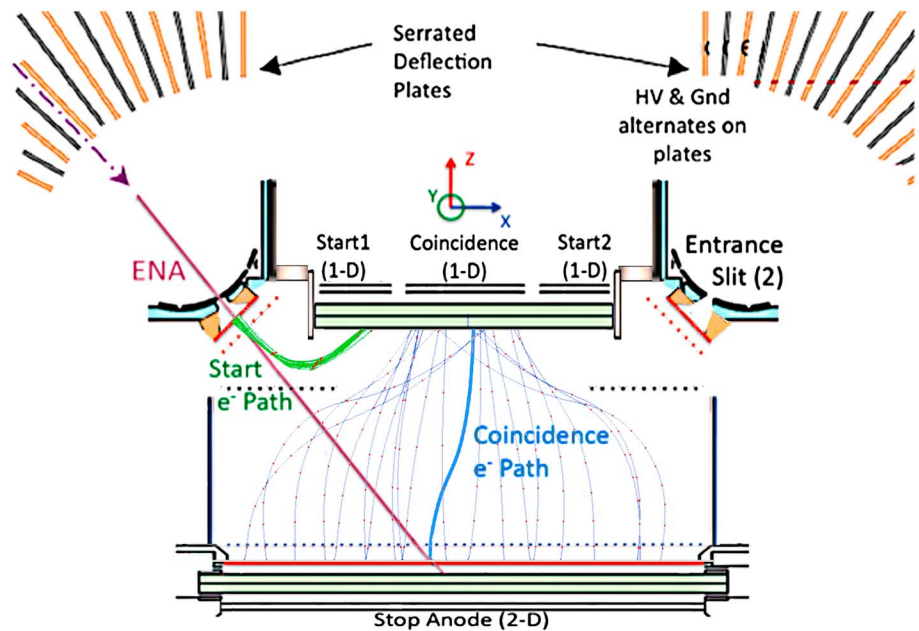
Figure 4. JENI's sensor optics provide high-resolution imaging coupled with accurate timing for effective background rejection.

these position timing pulses for the delays introduced by the time delay anode. The corrected start time is known to ~0.5 ns. Coincidence anode position (total delay ~60 ns) is accurate to ~2 mm and timing to ~0.5 ns.

3.4. Stop Assembly—MCP

The particle under analysis continues through the sensor volume to the stop foil and stop MCP (Figure 4, red horizontal line and bottom double green horizontal bars), producing both 2-D stop position and stop timing. The stop MCP is backed by a 2-D time delay anode with four readouts, two for position across the figure and two for position out of the figure plane. As in the case of the start anode, the TOF stop time is derived by correcting the position timing pulses for the anode delays, accurate again to ~0.5 ns. This stop position (~1 mm accuracy) and time together with the start position and start time uniquely determine the particle trajectory and TOF. As was done for INCA and HENA, the pulse height (PH; 8 bits is sufficient) from the stop MCP is recorded and, when paired with the TOF, yields a rough determination of particle species (either light—H, He, or heavy—O and S). Whereas on INCA and HENA the secondary electrons from the stop foil were collected by the stop MCP detector in addition to the ENA impact, our current intention is to back-bias the stop foil and record only the ENA impact. This choice is motivated by the need for high-position resolution, which can be degraded when both sources of signal are collected.
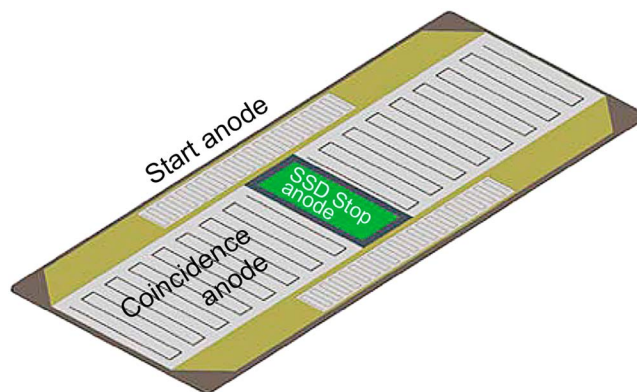

Figure 5. JENI's start and coincidence anodes provide excellent timing (~0.5 ns) and position (~1 mm). Start and coincidence anodes are time delay anodes; the coincidence anode is split into three sections, time delay above the stop MCPs, and discrete (green) above the SSDs.

3.5. Stop Assembly—SSD

The sensor back plane comprises two stop MCP assemblies, bisected by a row of SSD pixels also behind the stop foil. Particles that hit one of the SSD pixels do not produce a stop MCP timing or position pulse, but their position is known
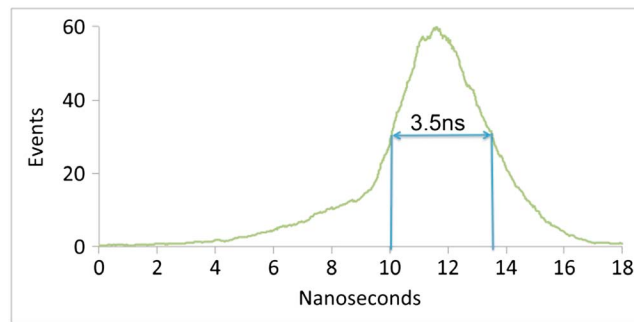
Figure 6. JENI's tight coincidence electron timing window provides a very strong coincidence timing constraint for valid events. For this laboratory test, the ~11.5 ns delay between stop and coincidence pulses was a consequence of laboratory cable lengths; however, the tight ~4 ns event window is independent of that setup timing offset. Events in the wings of this distribution (~1/3 of the total for this breadboard setup) would be declared invalid and not further processed.

from the location of the SSD pixel they enter, and the SSD returns their deposited energy. This energy, together with TOF derived from the start time and an SSD stop taken from the SSD portion of the coincidence anode (green rectangle in Figure 5), yields TOF × E, sufficient to identify the particle species (H, He, O, or S). This information produces species-separated images that inform the less precise composition obtained in the higher angular resolution, higher counting statistics images provided by the stop (MCP) detector measurements.

3.6. Coincidence Assembly

The JENI coincidence pulse is registered in a three-part anode (Figure 5) located behind the start-coincidence MCP, between the two time delay start anodes. Electrons backscattered from the foil covering the stop MCPs are accelerated and guided by the steering potentials onto the coincidence region of the start-coincidence MCP (Figures 4 (blue electron trajectories) and 5). The efficiency for producing these electrons, like the start electrons, is a function of incident particle energy. The Juno/Jupiter Energetic Particle Detector Instrument (JEDI) and Van Allen Probes Radiation Belt Storm Probes Ion Composition Experiment instruments rely on identical processes (though different electrostatic configurations), and those efficiencies have been carefully calibrated. Those results were included in the JENI counting rates and signal-to-noise results discussed below. Their travel time from the stop foil to the coincidence MCP varies between about 2 ns near the center of the instrument to about 4 ns near the edges of the back plane. Together with dispersion of the electrons caused by "thermal" velocities (we use the term thermal loosely here and below—the secondary electron distribution is not truly thermal but rather has characteristics determined by a variety of processes too detailed to discuss here—please refer to *Allegrini et al.* [2016] for a full discussion), the total window broadens to about 3.5 ns FWHM (Figure 6). The electron optics is designed to produce no forces in the dimension parallel to the slit entrances, so in that dimension the mapping from the stop position and the coincidence position (Figure 7) is nearly one to one (aside from spreading caused by the thermal energy of the backscattered electrons and slight displacements in the stop position for large angles of incidence).

For particles that penetrate the stop foil above the SSDs and deposit their energy in one of the SSD pixels, the backscattered electron trajectories lead to the SSD stop timing anode that bisects the two serpentine coincidence delay-line anodes (see Figure 5). These electrons, like those used in coincidence logic, take between 2 and 4 ns to reach the SSD stop section of the top detector; however, as noted above the electron travel time depends monotonically on position across the back plane, so that the appropriate correction for that travel time can be made based on identification of which SSD pixel was triggered by the particle. This correction can reduce the electron timing dispersion to ~1 ns, so that the SSD TOF (corrected time between the start and the SSD stop) is accurate to ~1.5 ns. This accuracy is sufficient to separate H, He, O, and S uniquely.

3.7. Electron Optics

JENI, like INCA and HENA before, relies on secondary electron acceleration and steering by electrostatic fields to achieve both accurate timing and the position resolution required for imaging ENAs. These electrostatic fields were developed using the program SIMION [e.g., *Dahl*, 2000], a program that uses iterative grid relaxation to solve for the electric potential in a three-dimensional volume with potentials specified on surfaces, and then implemented in a laboratory breadboard sensor and tested using alpha sources. The timing and position results in Figures 6 and 7 were achieved using that setup. Figure 8 shows the SIMION electrostatic potential contours (red) and electron trajectories for the start (green) and coincidence electrons (blue).
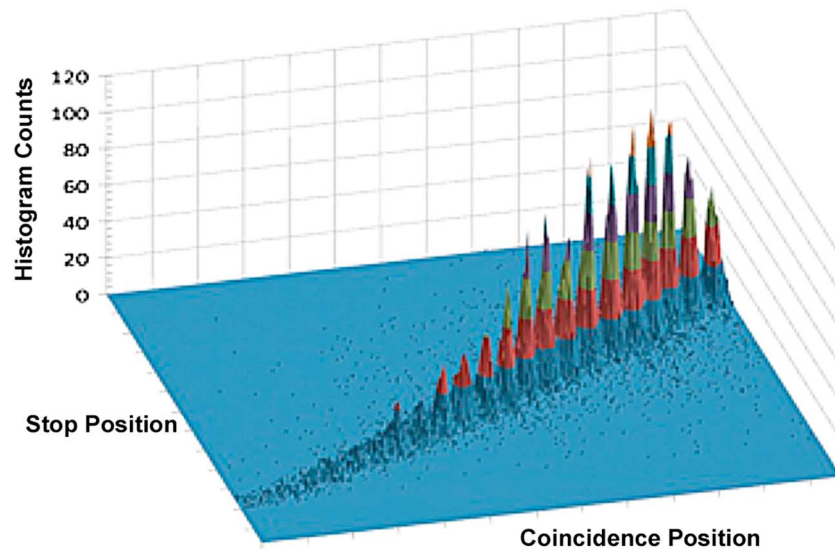
Figure 7. Well-controlled electrostatic fields (including control of fringing fields at the ends of the volume) provide nearly one-to-one mapping of stop to coincidence position, a requirement for acceptance as a valid event. Lab data show that a factor of at least 20 reduction in accidentals can be achieved by this mapping constraint.

Some of the control voltages are carried by extremely thin wires strung harp-like along the length of the sensor (and viewed end-on in Figure 8). The same approach was used in both HENA and INCA. These wire electrodes, along with some of the side electrodes that reside outside the region through which particles travel, end in insulated end walls. To eliminate fringing fields, those end walls include circuit board tracks that mimic the contours in the SIMION simulation and carry the same potentials as the SIMION contours by means of a resistor-divider chain powered by the MCP HV power supplies.

3.8. Foils

INCA and HENA used thin, grid-mounted foils in their entrance slits as well as covering the stop MCP. In HENA and INCA, these foils serve the dual purpose of producing secondary electrons as primary particles penetrate
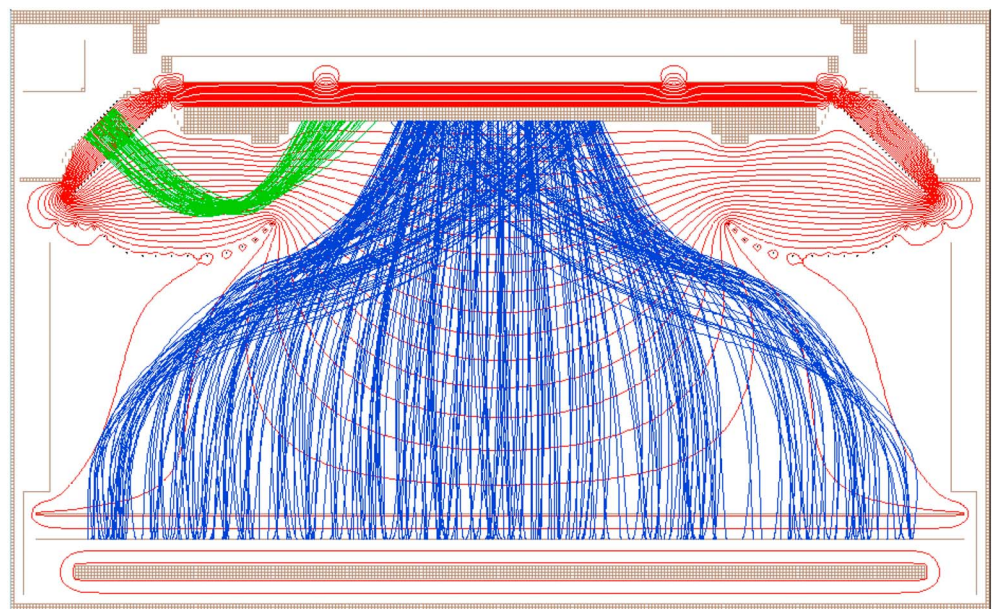

Figure 8. JENI's electrostatic fields control the start and coincidence electrons very effectively, resulting in low dispersion in position and time. Start electron trajectories appear in green, coincidence electrons in blue, and electrostatic potentials in red.

them, and blocking UV and visible light so that UV-generated photoelectrons do not swamp the MCP counting rates, and visible light does not increase noise levels in the SSDs. For HENA and INCA, the start foils were designed to reduce the FUV- and EUV-related counting rates to $\sim 10^4$/s or less, which in the case of INCA required an $\sim 10\,\mu g/cm^2$ start foil thickness, composed of silicon and Lexan, with a thin flashing of $1\,\mu g/cm^2$ carbon on the exit surface to provide conductivity (critical to maintaining its potential) and to provide a stable secondary electron emission surface. This foil reduced the FUV and EUV photon fluxes through the entrance slit by a factor of ~ 200. For HENA, in the brighter Earth environment, the start foil thickness was $15\,\mu g/cm^2$. The stop foils in each were $\sim 7\,\mu g/cm^2$, a sandwich of carbon, polyimide (Lexan), and carbon in HENA (INCA). This foil attenuated UV photons (primarily Lyman α) by another factor of ~ 50.

Of course, these foils could have been made even thicker, eliminating even more of the UV photon flux, but the thickness of the foils, particularly the start foil, limits the minimum energy ion or ENA that can penetrate both foils and reach the stop MCP. Furthermore, those particles that are sufficiently energetic to penetrate the start foil are scattered in angle and lose some energy in transiting, so the thinner the foil, the lower the energy loss and the less the scattering.

The JENI approach to the thin start foils is to eliminate the requirement that they act as photon filters. Despite the lack of filtering of UV, in some of the Jovian environments that JENI will encounter, the MCP counting rates will not be dominated solely by UV photoelectrons (predicted detector rates in ENA mode for UV photons at Jupiter are $\sim 10^5$/s), but by also by foreground plasma electrons above the collimator plate sweeping energy (or in ion mode all the plasma electrons), as well as by penetrating radiation (also primarily electrons). So filtering the UV photons would not materially improve the sensor performance.

Therefore, the JENI start foils, relieved of any requirement on UV suppression, may be made as thin as feasible, consistent with surviving launch and providing a source of secondary electrons. Traditional plasma analyzers routinely use grid-mounted carbon foils of 1 to $2\,\mu g/cm^2$ thickness, and the IBEX-Hi ENA instrument employs foils $\sim 0.6\,\mu g/cm^2$ covering its entire aperture of $156\,cm^2$, tiled in individual foils each $\sim 10.5\,cm^2$. These survived launch intact despite including no acoustic cover and continue to function nominally after 8 years in orbit. Both MENA and TWINS instruments also flew such ultrathin foils in a configuration somewhat similar to that anticipated here. Based on this experience as well as laboratory test, for JENI we plan to use $\sim 1\,\mu g/cm^2$ start foils on each entrance. The variable aperture mechanism also provides the option to insert a much thicker UV, and visible, photon filter ($22\,\mu g/cm^2$ of aluminum and palladium) to allow continued operation in direct sunlight (at the cost of minimum particle threshold of $\sim 10\,keV$ for protons, $60\,keV$ for oxygen, and $100\,keV$ for sulfur).

JENI's stop foil need not reduce the UV intensity for the stop MCPs either, as the number of UV photons reaching them is no greater than the flux leaving the exit surface of the start foils (less grid transmissions), and so UV-generated rates on the stop will be no higher than on the start. So this foil also is $1\,\mu g/cm^2$ carbon, supported on ~ 300 line/inch grid (measured to have 73.4% transmission in the case of IBEX-Hi [*Funsten et al.*, 2009]). Given the size of the stop foil(s), this may be a technical challenge. Should this approach encounter problems during development of the EM, our fallback position will be to use a stop foil patterned on the INCA or HENA stop foil as described above. The only performance degradation associated with that fallback would be to raise the minimum energy threshold for hydrogen to $\sim 2\,keV$ and for oxygen to about $10\,keV$. Because the start and stop/coincidence foils are not used as photon filters, our design is highly tolerant to loss of foil area to broken grid cells that may occur during launch or in manufacture or handling. Individual cell loss affects only sensitivity (sensor efficiency), so lost foil area on the order of 10% or even more has only minor impact on science.

Over the SSDs JENI includes a foil designed to reduce the UV and visible light reaching the SSDs sufficiently to eliminate light-induced electronic noise and increased leakage current.

We have carefully modeled the expected UV-induced rates on start, stop, and coincidence detectors based on measured interstellar hydrogen Lyman α, Jupiter system measurements from Voyager and Cassini, and solar UV reflected from Ganymede using the Ganymede surface albedo, and for our largest slit aperture setting they remain below $\sim 2 \times 10^5$, $\sim 1.5 \times 10^5$, and 1.3×10^5, respectively—well below expected rates from foreground electrons at Ganymede or Europa. The rates reduce linearly with slit area for the lower sensitivity, higher angular resolution apertures. It should be noted that these UV levels are relatively modest compared with typical environments near Earth.
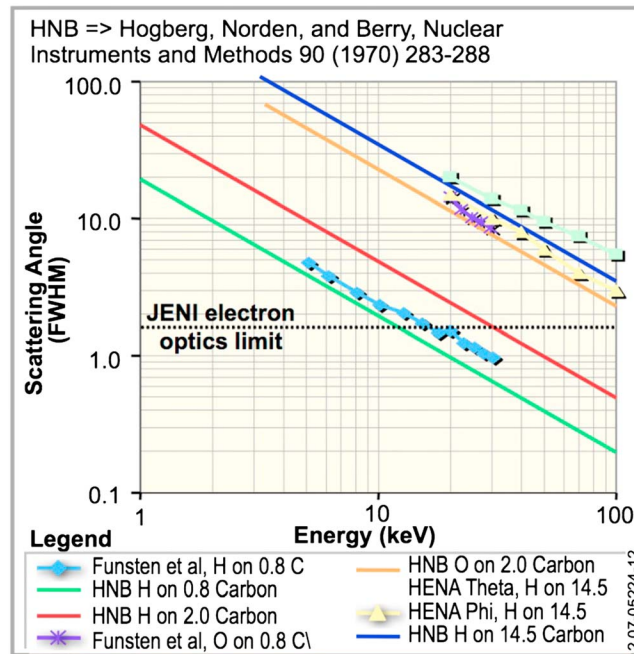
Figure 9. JENI's thin foils and electron optics provide better than 2° angular resolution above scattering-dominated energies, with resolution still better than INCA's best as low as 5 keV for protons. The references to Funsten et al. are to the 1993 paper in the reference list. The references to, e.g., 0.8 carbon are to a nominally 0.8 μg/cm² carbon foil (thin foils typically also include ~1 μg/cm² additional material, mostly adhered water). The reference to 14.5 without a material stated is to the HENA start foil, which totaled ~14.5 μg/cm² material, in layers of carbon, polyimide, and silicon.

4. Performance

4.1. Angular Resolution, Energy Threshold

The minimum energy threshold for hydrogen, based on the energy at which hydrogen penetrates both start and stop MCP foils, is ~0.5 keV, for oxygen ~4.0 keV, and for sulfur ~8.0 keV (these are the energies for which 50% of the incident particles transit both foils [according to TRIM, the software developed by *James F. Ziegler*, *"The Stopping and Range of Ions in Solids,"* Pergamon Press (1985). Among other capabilities, this software package calculates a large range of parameters for the interaction of energetic ions with solids, including energy loss and scattering.]). For the SSD section, taking into consideration energy loss in the dead layer and detector noise the lowest TOF × E analysis begins at ~30 keV for hydrogen, 70 keV for oxygen, and 120 keV for sulfur.

Angular resolution for ENA imaging is limited primarily by two factors: the scattering of the particles as they transit the start foil and the precision of the electron optics, in particular the start electron trajectories as they deviate from ideal trajectories because of random thermal velocities of the secondary electrons released from the foil surfaces. The MCP imaging resolution is sufficiently high that it does not impact image resolution substantially.

In order to attain the goal of ≤2° angular resolution, it is important to control the spread of the secondary electrons emitted from the start foil during their transit to the start MCP. The secondary electron path length from the start foil to the start MCP is ~3 cm. The typical thermal energy of a secondary electron is 3 to 4 eV for the backward scattered electrons. This thermal energy is directed almost randomly relative to the foil surface, with a broad peak perpendicular to the foil. Using a nearly worst case of 4 eV directed parallel to the imaging dimension (**Y**; out of the plane of Figure 4), and assuming an acceleration voltage of 1 kV as in our lab prototype of JENI, the ratio of the thermal to accelerated velocities is roughly $\sqrt{(E_{th}/E_{potential})} = 0.063$. So the thermal smearing in **Y** should introduce an uncertainty of <0.063 × 3 cm or <01.9 mm (worst case). The full width at half maximum uncertainty, when the full thermal distribution is considered, is more like 1 mm. This is sufficient for the required angular resolution. The mapping from the stop foil to the coincidence MCP involves a somewhat longer flight path (4–6 cm), as well as a lower average energy for the secondary electrons, so that mapping is expected to be accurate to within ~2.5 mm (discussed in greater detail in the next section).

Above 15 keV for hydrogen and about 150 keV for oxygen, scattering in JENI's very thin entrance foils no longer dominate JENI's angular resolution (see Figure 9; representing results from *Högberg et al.* [1970] and *Funsten et al.* [1993]). The thermal spread of secondary electrons discussed above limits the angular resolution to about 1.6° above those energies. Below those energies foil scattering dominates, but for hydrogen the angular resolution is still very good (about 5° FWHM at 5 keV incident energy) and predicted to be ~20° FWHM at 1 keV. For oxygen resolution is expected to be ~10° at 20 keV and ~20° at 10 keV total energy. Thus, JENI's angular resolution is far better than INCA or HENA, allowing for the imaging of magnetospheric hot plasma structures that would be left unresolved by INCA or HENA.

4.2. Radiation and UV Background Mitigation—Valid Event Logic

Our approach to background rejection is to use a combination of sufficient shielding on the sensor to reduce detector rates to levels that can be handled by the detector front end electronics without count rate saturation and, for environments in which the detector rates remain above those levels, to raise the detection threshold for the MCP pulses sufficiently to lower the rates to manageable levels. We then follow the front-end signals with fast valid event logic sufficiently robust to identify valid events and use them to produce telemetry products (ENA images, ion angular distributions, and spectra) while rejecting background events.

For HENA and INCA the primary source of detector background was UV, which we mitigated by designing the start foil as a UV filter. This begs the question how can we use such a very thin start foil in JENI, maintain a high geometric factor, and still reject the UV flux adequately? It requires a valid event design that does not depend on the front foil for UV attenuation. In JENI we have a front foil of thickness $\sim 1 \, \mu g/cm^2$ and a geometry factor in the same range as the INCA and HENA sensors. With TOF-only valid event logic (used successfully in HENA and INCA), the expected accidental rate is $A = R_{start} \times R_{stop} \times \tau$ (where R_{start} is the combined EUV, penetrating particle, and foreground start MCP counting rate, about $3 \times 10^4/s$ typically; R_{stop} is the same for the stop MCP, about $2 \times 10^3/s$; and τ is the maximum allowable TOF—the valid event window, which for HENA was 100 ns). So for HENA $A = 3 \cdot 10^4 \times 2 \cdot 10^3 \times 10^{-7} = 6/s$, consistent with on-orbit performance.

Applying the formula above to JENI (which has no EUV filtering by the start foil), photoelectrons, foreground electrons, and penetrators together dominate start, stop, and coincidence rates. For example at Ganymede where penetrating background stop rates are modeled using Geant4 (a toolkit for the simulation of the passage of particles through matter [*Agostinelli et al.*, 2003; *Allison et al.*, 2006]) at $4 \times 10^5/s$, start rates at $2 \times 10^5/s$ and with $\tau = 220 \, ns$ (longer than HENA to accommodate the low-energy end of the ENA range), accidentals would be $A \sim 2 \cdot 10^5 \times 4 \cdot 10^5 \times 2.2 \cdot 10^{-7}$ or $\sim 1.8 \times 10^4/s$, unacceptably high.

JENI has a total of four (one spatial and three timing) coincidences to mitigate the detector backgrounds caused by UV, by penetrating electrons, and by electrons entering through the aperture above the deflection system cutoff (at about 300 keV in ENA mode to as low as zero in ion/electron mode with the deflection system HV off). Thus, background from accidental, false valid events is strongly suppressed in this instrument by (1) adding a second, even tighter coincidence time constant $\sim 4 \, ns$ and (2) only accepting events for which coincidence positions agree with the particle stop positions (as discussed above).

Because valid events that hit the stop foil must produce correlated pairs of positions in the stop and coincidence MCPs, events may be declared invalid if the two positions do not correspond. For the projection shown in Figure 7, the valid event decision is based on the 1-D position correlation perpendicular to that plane. That is, particles that penetrate the stop foil and produce a position in the stop MCP also generate coincidence electrons (blue trajectories) that produce a timing pulse and a position (in the dimension perpendicular to the figure) in the coincidence anode, above. The two positions must agree for an event to be considered valid.

The new formula for false valid events becomes $A_{MCP} = (R_{start}) \times (R_{stop}) \times (R_{coin}) \times \tau_{TOF} \times \tau_{Coin}/N_{positions}$, where R_{coin} is the coincidence anode total rate, τ_{coin} is the stop-coin timing window, and $N_{positions}$ is the number of independent positions that the coincidence electron mapping permits to be mapped between stop and coincidence anodes. Using numbers for Ganymede foreground and background electron spectra from *Jun et al.* [2005], and UV intensities based on multiple sources, this yields $A_{MCP} = 2 \cdot 10^5 \times 4 \cdot 10^5 \times 4 \cdot 10^5 \times 2 \cdot 10^{-7} \times 4 \cdot 10^{-9}/20$ or $\sim 2.5/s$ (where each term is identified with the corresponding term in the expression at the beginning of the paragraph).

So despite the intense backgrounds and foreground electrons, as well as the very high detector counting rates, the strict timing and spatial coincidence criteria on JENI result in exceeding low false valid event rates. To compare with the MENA approach, according to *Pollock et al.* [2000], at Earth for IMAGE MENA the predicted rates (start + stop) with the transmission grating in place would be $\sim 200/s$, divided evenly between start and stop. The grating was measured to have a transmission of $\sim 10^{-5}$ at Lyman α, rising to $\sim 10^{-2}$ at 30 nm. The 200/s rate on MENA is dominated by the short-wavelength part of the spectrum, so if all the UV were allowed in, that rate would go to $2 \times 10^4/s$ from the short-wavelength portion of the spectrum, with probably a roughly equal contribution from Lyman α (higher intensity but lower efficiency), or $\sim 4 \times 10^4/s$ for start + stop. For a 100 ns TOF window, that would have resulted in an accidental rate of $\sim 40/s$. The MENA

geometric factor is very roughly ~0.01 cm^2 sr based on an effective area of ~0.1 cm^2 exposed to a solid angle formed by the deflection system FWHM of ~4° by an acceptance in the other dimension of about 110° (see *Henderson et al.* [2005] for a complete discussion). For the approach we are taking, removing the gold grating filters in MENA would increase the geometric factor (GF) by about a factor of 20 to 0.2 cm^2 sr for an otherwise similar instrument. In the configuration we envision, this would be achieved by opening up the second angle (the spin angle in MENA, constrained both by the deflection plate system and the gold gratings). Then the start and stop rates would be up by an additional factor of 20 to ~8×10^5/s, and without the additional coincidence we employ the predicted accidental rate would be ~8×10^5/s $\times 8 \times 10^5$/s $\times 100$ ns = ~6.4×10^4/s, still much too high. If we calculate accidentals using the coincidence approach we are suggesting, the rate would be ~8×10^5/s $\times 8 \times 10^5$/s $\times 8 \times 10^5$/s $\times 100$ ns $\times 4$ ns/20 = ~10/s. So our approach to a MENA-sized instrument would result in 20 times the sensitivity with an accidental rate of only 10/s. However, since 8×10^5/s is a very high single rate, we would design for a somewhat smaller geometric factor, perhaps by a factor of 3 smaller, for the Earth environment where the UV intensity is between 1 and 2 orders of magnitude higher than at Jupiter. Then the single rates would be down to ~2.67×10^5/s, bringing the accidental rate down to ~0.4/s. Were we to include the variable aperture mechanism employed for our JENI instrument, we could design the maximum geometric factor to be larger (for example, 0.5 cm^2 sr) and reduce the aperture when UV rates required it.

Likewise, the TOF$\times E$ measurement using the SSD in combination with the coincidence pulse as the SSD TOF stop pulse yields very low accidental rates for ion and neutral composition. The SSD version of the accidental formula $A_{SSD} = R_{start} \times R_{SSD} \times R_{SSD-TOF} \times \tau_{TOF} \times \tau_{SSD}$ yields (term for term) $A_{SSD} = 2 \cdot 10^5 \times 2 \cdot 10^4 \times 2 \cdot 10^4 \times 1 \cdot 10^{-7} \times 1 \cdot 10^{-6}$ or ~0.8/s, where $R_{SSD-TOF}$ is the rate on the solid section of the coincidence anode that serves as the SSD TOF stop pulse and τ_{SSD} is the pulse-shaping time constant for the SSD pixels. Again, the strong coincidence requirements constrain the valid event criteria sufficiently to result in exceedingly low background rates for valid events.

The foreground electrons (electrons entering the slit aperture) do present a significant problem in the Ganymede and Europa environments. With the geometric factor set to 1, for example, over 10^7 electrons per second would enter the instrument. In calculating valid events using the coincidence criteria, we have assumed individual MCP detector single rates in the 2 to 5×10^5 range. This is OK, as long as the efficiency of these detectors for the foreground electrons is not too high. The efficiencies for secondary electron production by energetic electrons at the surfaces of the thin foils that JENI uses is very low (~1% or less), so these electrons will not drive excessive rates on the start or coincidence MCPs that do not view the incoming electrons directly. For the stop MCPs, the efficiency may be as high as 30% to 50% for these electrons, which would result in single rates beyond the capability of the front-end electronics. So while such a large geometric factor can be used for spacecraft positions outside the central plasma disk, near the center of the plasma disk a smaller geometric factor may be required to avoid overwhelming the front-end electronics. This means dialing the geometric factor down until the detector rates are reduced to $\sim <10^6$/s. The required geometric factor (GF) will vary depending on mission phase, but at Ganymede a GF < 0.2/cm^2 sr will be needed (unless, as discussed below, we take other measures to reduce the stop MCP rates).

4.2.1. Implications for Front-End Speed

We use time delay anodes for which the time delays in the 1-D coincidence anode are matched to the time delays in the stop anode for the dimension parallel to the slit. In this way, a direct comparison of the time of arrival of the pulses from the stop and coincidence anodes can be made, allowing this valid event criterion to be applied in less than 400 ns. If the 1-D correlation criterion is met, the event can be accepted as valid. The logic for this decision is programmed into a field-programmable gate array (FPGA), which is capable of fast logic and can reject events before they reach the data processing unit (DPU). If the positions are consistent, they are called valid in the FPGA logic and passed on to the DPU for event telemetry. If they are not consistent, the event is rejected and never gets sent to the DPU. Total live time and dead time are tracked and in addition a technique by which a predetermined rate of valid (but pulser initiated) events goes through the same set of bottlenecks as the real data allow for rate correction (pileup correction).

The spatial coincidence technique for mitigating high background rates will require, in particular, fast position sensing on the start, coincidence, and stop MCP-anode systems. With projected rates on the start MCP expected to range as high as 1 MHz, the position must be measured in well under 1 μs. There are several

techniques that can achieve position measurement with adequate resolution for this application, in the space of ≤100 ns for the measurement itself, with an additional ~300 ns dead time before the next measurement. JENI uses a delay-line anode, which measures the time delay between the arrival of the MCP output pulse at opposite ends of the anode. APL's new flight-qualified TOF application-specific integrated circuit (ASIC), an improved version of the very low power, rad-hard TOF-A chip used to measure the ENA TOF in the HENA instrument, is used on the output of 1-D and 2-D delay-line anodes. These can provide the 1-D start position in ~400 ns (including chip reset dead time). The TOF ASIC measures the time difference between the arrival at the chip of the signal from the two ends of the time delay position sensitive anode. From that time difference the position of the event can be determined to ~1 mm in this implementation.

4.2.2. Pulse Height Thresholding

There is a different way to cut down the counting rates caused by penetrators, foreground electrons, and UV and that is to increase the pulse height (PH) detection threshold on the MCP detectors (or alternatively to reduce the MCP voltage and so reduce its gain such that smaller pulses are no longer detected above threshold). Most penetrating background electrons as well as UV and foreground electrons all produce small (single-electron or smaller) MCP pulses, whereas a fraction of the hydrogen and virtually all heavier ions typically produce larger, multiple-electron pulses. By setting the detection threshold above the single-electron pulse height, a tunable fraction of the background and foreground electron counts will be eliminated, reducing detector counting rates by as much as a factor of 10 and (because they result from the product of the individual detector rates) reducing accidentals by much larger factors. Because many protons produce only a single secondary electron, sensitivity for hydrogen is significantly reduced, but for He, O, and S sensitivity is only minimally affected, and a large geometric factor can be chosen, even at Europa and Ganymede.

A further refinement of this approach is likely to be quite effective in the Ganymede and Europa environments, a refinement that will have a much smaller impact on hydrogen efficiency. As ions or ENAs pass through thin foils, the number of secondary electrons produced at the entrance and exit surfaces of the foils depends on the dE/dx of the incident particle in the foil material. Simply put, the greater the dE/dx is, the more electrons within a short distance of the foil surface are energized to the point that they can escape the material. For incident particles in the keV to hundreds of keV range, typical secondary electron yields vary between about 1 to 3 for hydrogen, 2 to 5 for helium, and 7 to 10 for oxygen and sulfur (see *Meckbach* [1975] for detailed discussions). Yields in the forward direction (exit side of the foil) slightly exceed those in the backward direction, especially in the case of hydrogen. In particular, for hydrogen the average electron yield drops below 1 for backscattered electrons below about 3 keV incident energy, peaks at ~3 around 80 keV, and drops below 1 again above about 800 keV. Forward yields are typically higher by a factor of about 1.5.

However, particles that reach the stop MCP produce a larger PH than the signals they create in the start and coincidence detectors. Consider the case of a 10 keV proton—as it exits the start foil it will yield two to three electrons, but in keeping with a Poisson process, it could also be one or four electrons. As it enters the stop foil, it will produce a typical one to two electrons (could be zero or three). As the particle exits the stop foil and strikes the stop MCP surface, it again typically produces two to three secondary electrons at the exit surface; these are accelerated into the stop MCP surface below the foil and generate an MCP pulse. The primary particle also generates an MCP pulse as it strikes the MCP surface in a slightly different location, and since the distance from the foil to the MCP is small, the two signals come so close in time and location that the anode and electronics see them as a single pulse. However, now the pulse reflects the sum of the foil and direct-hit MCP pulses or equivalent to a three- to five input-electron signal.

This is very different from what most electrons (foreground or penetrating) or UV photons will generate. Those background sources will generate primarily a single-electron pulse or smaller. A UV photon is destroyed in the process of generating a photoelectron and so will produce no more than a single-electron pulse. An electron has a very low dE/dx and so a low probability of generating even a single electron in a foil; because at high energies they can penetrate the MCP glass and so have the potential to energize any of multiple channels, those high-energy electrons have a much higher efficiency for triggering the MCP and can generate large pulses but typically produce only a small PH. So by raising the electronic threshold on the stop MCP above the single-electron peak, most of the background response disappears, while the ions and/or ENAs (especially oxygen and sulfur but even hydrogen as the discussion above indicates) will still produce a response above threshold.
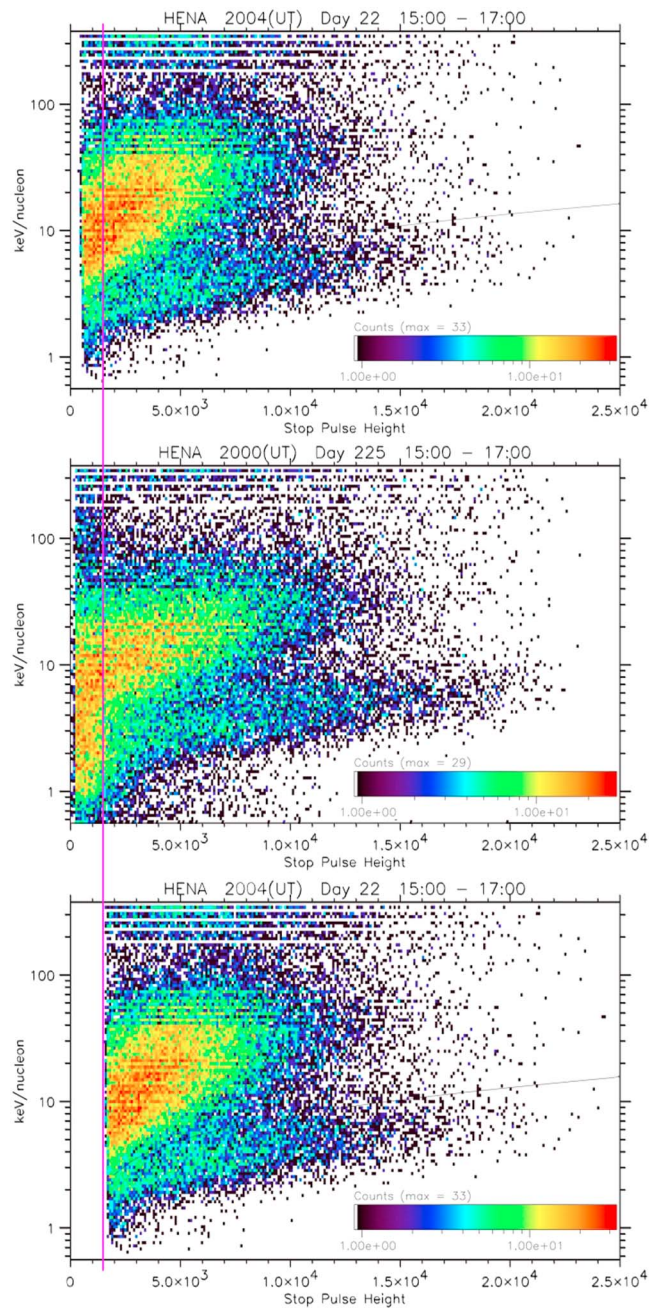
Figure 10. JENI will use MCP pulse height to separate hydrogen from heavier ions (oxygen and sulfur and to discriminate against background sources (foreground electrons, penetrating electrons, and UV). The plots above are examples of ENA stop MCP pulse height distributions versus particle energy (in keV/nucleon) from the IMAGE HENA instrument for large geomagnetic storms: (top) January 2004 and (middle) August 2000. (bottom) The same January 2004 data shifted to the right to match the August 2000 pulse height distribution. The vertical pink line is a virtual threshold for reference.

HENA data in Figure 10 demonstrate this feasibility. The ENA PH distribution in the middle plot was recorded in a large geomagnetic storm in 2000, not long after the IMAGE launch when the HENA MCP gain was high. The PH distribution at the top was in a similar storm in 2004, when the MCP gain had diminished, and the PH threshold had also been raised.

In the middle plot, for the small PH points to the left of the vertical guide line the distinction between H (upper diagonal cluster) and O (lower, more horizontal cluster) is blurred. In the bottom plot, we repeat and shift to the right the data from the top plot (for which the MCP gain had degraded a little). The data were shifted to the right sufficiently that the H and O PH distributions in 2000 and 2004 appear self-similar, which should compensate for the drop in MCP gain between those epochs. We then drew the vertical line through the plots at the threshold of the shifted 2004 data, under the assumption that in 2004 the single-electron peak was below the stop PH threshold. The low PH data to the left of the line in the middle plot are dominated by accidentals caused by energetic electrons (there was no electron sensor aboard IMAGE to confirm this, but they are not unusual in Earth's magnetosphere in a large geomagnetic disturbance).

Note that by effectively changing the PH threshold on the stop MCP we have eliminated the small PH points that are suspect because of their peculiar distribution, yet in doing so we have made very little impact on eith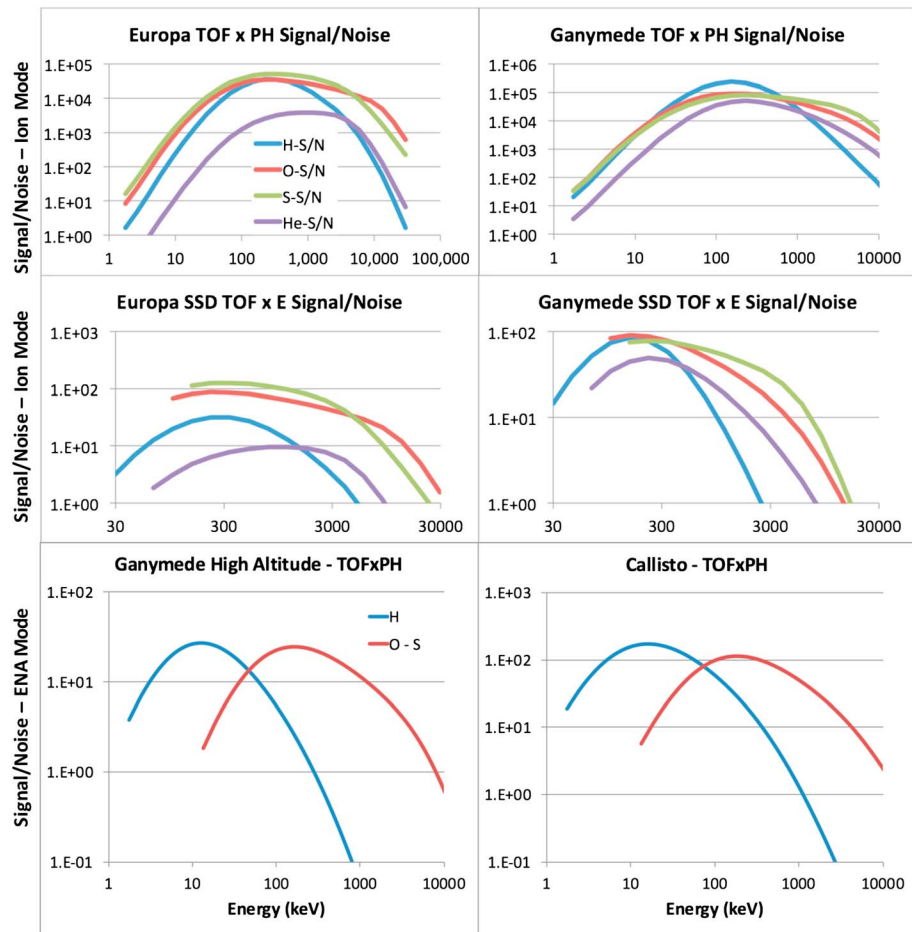er the hydrogen or the oxygen efficiencies. Most of the hydrogen events remain in the more intense, diagonal cluster of points at higher energy per nucleon. Some real hydrogen data are lost in this process; the diagonal H distribution clearly extends to the left of the threshold line in the middle plot, when the MCP gain was higher and the threshold was lower. But the loss of efficiency is still less than 50%. In this argument we have focused only on the stop MCP. Because of the double signal provided by the stop foil and the stop MCP itself, raising the threshold on the stop MCP

Figure 11. The JENI background rejection approach results in high signal-to-noise ratios (SNRs) throughout its energy range. For the most severe background environments (Europa, Ganymede open field lines), PH thresholding reduces hydrogen sensitivity (included in SNR shown). (top middle) SNR for MCP-only (ToF$_{SSD} \times E$) ions based on our triple coincidence and PH thresholding. (bottom) SNR for ENA mode, imaging of the Jovian magnetosphere from these locations. The primary products for this mode will be TOF $\times$ PH, so only those are shown. Oxygen and sulfur will not be distinguishable in this mode.

anode has a large effect on the small background pulses while having a small effect on the ions (almost none on He, O, and S and very modest on H). At Ganymede and Europa, the highest detector rates are expected to be driven by foreground electrons entering JENI though the entrance slit apertures. As mentioned above, we can control that by stopping down the apertures, but because the response to these direct electrons is considerably stronger in the stop MCP than in the start or coincidence, tailoring the stop PH threshold to discriminate against the single-electron PH is the most desirable course of action to mitigate high background rates from foreground electrons.

Other considerations in this argument are (1) whether even if we are not triggering the front-end event circuits, can the MCP itself keep up with the background rates and (2) is the pulse shaping time for the MCP amplifiers sufficiently short that they do not suffer from pulse pileup?

At ~10^7 el/s entering the instrument there is the potential for the stop MCPs to be generating roughly 1/2 to 1/3 that number of pulses/s. For the MCP itself, this should not be a problem. Each stop MCP has an area of approximately 44 cm^2, so the rate per cm^2 would be on the order of 7×10^4/cm^2/s, a rate any reasonably high rate MCP can sustain (for example, the start MCP on INCA frequently reaches nearly 10^6/s in Saturn's radiation belts with no ill effects, and it is a fairly low-rate MCP with an area of only 15 cm^2). This corresponds to an extracted charge of less than 1 C/cm^2 from our JENI MCPs over the duration of the mission. This is far below
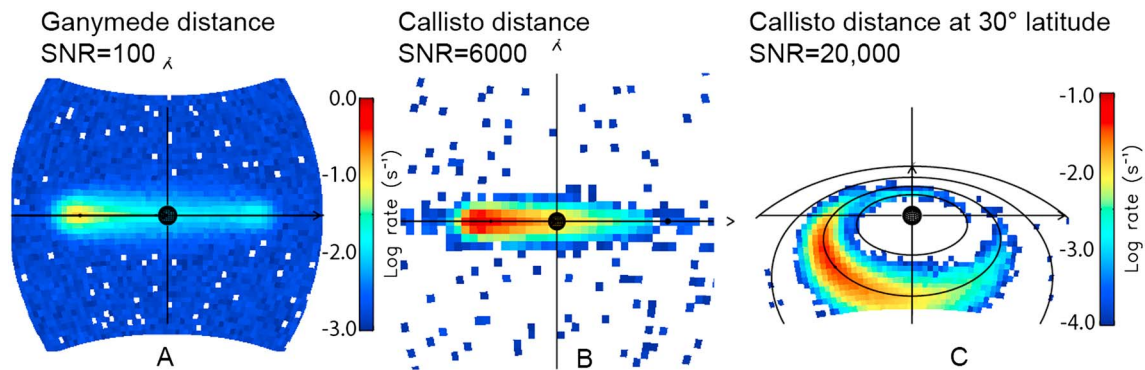
Figure 12. Simulated ENA images of the inner magnetosphere: (a) worst-case conditions at Ganymede, (b) at Callisto's orbital distance, and (c) during high-inclination phase. To ensure clean ENA images, JENI has implemented a triple coincidence system plus a pulse-height (PH) rejection scheme. PH rejection cuts background single rates by ~1/4, sufficiently that counting rates remain unsaturated. Triple coincidence yields a SNR ~100 even at Ganymede. PH rejection need not be used at Callisto's distance.

the $40 \, C/cm^2$ limit specified by Photonis or the $8 \, C/cm^2$ to which we have tested our EM plates, and therefore, there is no risk of premature MCP aging.

As for pulse shaping, at $10^7/s$ one would want a pulse shaping time constant of ~30 ns to avoid pulse pileup; JENI's MCP amplifier time constants will be considerably shorter than that, given the need for ~1 ns time resolution for the timing and position pulses.

In cases where all of the MCPs are counting at rates above what the front-end electronics can handle, we can use the technique of raising the MCP PH thresholds on the start and/or coincidence anodes in addition to the stop. In that case, as in the case of ACE/ULEIS, the hydrogen efficiencies will be impacted, but JENI will still produce high-quality scientific data. There is no risk for SSD pileup since we adjust our collimator size to keep rates below 10^5 counts/look SSD channel; performance at this rate has already been demonstrated on our Juno/JEDI electronics (which is our baseline for both Jovian Energetic Neutrals and Ions and Jovian Energetic Electron energy channels).

4.3. Foreground/Background, Signal/Noise Simulations

Simulations of the JENI S/N have been carried out under conditions expected at various locations in Jupiter's magnetosphere. Figure 11 provides a summary of those simulations, based on the background rejection techniques discussed above.

Figure 12 shows the results of simulations of images in different regions of Jupiter's magnetosphere, with modeled signal to noise characteristics based on the background rejection techniques discussed above.

5. Summary

We have developed several techniques that allow us to improve upon the performance characteristics of former high-energy neutral atom instruments (specifically, HENA and INCA). These techniques include fast, multiple timing coincidence detection and valid event logic, spatial coincidence valid event logic, and the application of pulse height thresholding (previously used in high-energy suprathermal ion instruments [e.g., *Mason et al.*, 2008]) to ENA sensors. These techniques allow imaging to lower energies (≤1 keV for hydrogen) and with higher angular resolution (~2° above 10 keV for hydrogen) than was previously possible on HENA and INCA. The techniques also allow us to make high signal-to-noise images in environments as severe at the Jovian magnetosphere in the vicinity of Ganymede.

References

Agostinelli, S., et al. (2003), Geant4—A simulation toolkit, *Nucl. Instr. Meth. Phys. Res. A*, *506*, 250–303, doi:10.1016/S0168-9002(03)01368-8.
Allegrini, F., R. W. Ebert, and H. O. Funsten (2016), Carbon foils for space plasma instrumentation, doi:10.1002/2016JA022570.
Allison, J., et al. (2006), Geant4 developments and applications, *IEEE Trans. Nucl. Sci.*, *53*(1), 270–278, doi:10.1109/TNS.2006.869826.

Brandt, P. C., K. Dialynas, I. Dandouras, D. G. Mitchell, P. Garnier, and S. M. Krimigis (2012), The distribution of Titan's high-altitude (out to ~50,000 km) exosphere from energetic neutral atom (ENA) measurements by Cassini/INCA, *Planet. Space Sci.*, *60*(1), 107–114, doi:10.1016/j.pss.2011.04.014.

Burch, J. L. (2000), IMAGE mission overview, *Space Sci. Rev.*, *91*, 1–14, doi:10.1023/A:1005245323115.

Dahl, D. A. (2000), SIMION for the personal computer in reflection, *Int. J. Mass Spectrom.*, *200*(1–3), 3–25, doi:10.1016/S1387-3806(00)00305-5.

Dialynas, K., S. M. Krimigis, D. G. Mitchell, E. C. Roelof, and R. B. Decker (2013), A three-coordinate system (ecliptic, galactic, ISMF) spectral analysis of heliospheric ENA emissions using Cassini/INCA measurements, *Astrophys. J.*, *778*(1), 40, doi:10.1088/0004-637X/778/1/40.

Funsten, H. O., D. J. McComas, and E. E. Scime (1993), Low-energy neutral-atom imaging techniques, in *SPIE Vol. 2008 Instrumentation for Magnetospheric Imagery II*, pp. 93–104, doi:10.1117/12.147647.

Funsten, H. O., et al. (2009), The Interstellar Boundary Explorer High Energy (IBEX-Hi) neutral atom imager, *Space Sci. Rev.*, *146*, 75–103, doi:10.1007/s11214-009-9504-y.

Gruntman, M. (1997), Energetic neutral atom imaging of space plasmas, *Rev. Sci. Instrum.*, *68*(10), 3617–3656, doi:10.1063/1.1148389.

Henderson, M. G., M. F. Thomsen, R. Skoug, M. H. Denton, R. Harper, H. O. Funsten, and C. J. Pollock (2005), Calculation of IMAGE/MENA geometric factors and conversion of images to units of integral and differential flux, *Rev. Sci. Instrum.*, *76*, 043303, doi:10.1063/1.1884190.

Högberg, G., H. Nordén, and H. G. Berry (1970), Angular distributions of ions scattered in their carbon foils, *Nucl. Instrum. Methods*, *90*, 283, doi:10.1016/0029-554X(70)90682-8.

Jun, I., H. B. Garrett, and R. W. Evans (2005), High-energy trapped particle environments at Jupiter: An update, *IEEE Trans. Nucl. Sci.*, *52*, 2281–2286, doi:10.1109/TNS.2005.860747.

Krimigis, S. M., et al. (2005), Dynamics of Saturn's magnetosphere from MIMI during Cassini's orbital insertion, *Science*, *307*(5713), 1270–1273, doi:10.1126/science.1105978.

Krimigis, S. M., D. G. Mitchell, E. C. Roelof, K. C. Hsieh, and D. J. McComas (2009), Imaging the interaction of the heliosphere with the interstellar medium from Saturn with Cassini, *Science*, *326*(5955), 971–973, doi:10.1126/science.1181079.

Krimigis, S. M., et al. (2004), Magnetosphere Imaging Instrument (MIMI) on the Cassini mission to Saturn/Titan, *Space Sci. Rev.*, *114*(1–4), 233–329, doi:10.1007/s11214-004-1410-8.

Mason, G. M., A. Korth, P. H. Walpole, M. I. Desai, T. T. Von Rosenvinge, and S. A. Shuman (2008), The Suprathermal Ion Telescope (SIT) for the IMPACT/SEP investigation, *Space Sci. Rev.*, *136*, 257–284, doi:10.1007/s11214-006-9087-9.

McComas, D. J., et al. (2009a), IBEX—Interstellar Boundary Explorer, *Space Sci. Rev.*, *146*, 11–33, doi:10.1007/s11214-009-9499-4.

McComas, D. J., et al. (2009b), The Two Wide-angle Imaging Neutral atom Spectrometers (TWINS) NASA mission-of-opportunity, *Space Sci. Rev.*, *142*, 157–231, doi:10.1007/s11214-008-9467-4.

Meckbach, W. (1975), Secondary emission from foils traversed by ion beams, in *Beam-Foil Spectroscopy*, vol. 2, edited by l. A. Sellin and D. J. Pegg, pp. 577–592, Plenum Press, New York.

Mitchell, D. G., et al. (2000), High energy neutral atom (HENA) imager for the IMAGE mission, *Space Sci. Rev.*, *91*(1/2), 67–112, doi:10.1023/A:1005207308094.

Mitchell, D. G., et al. (2005a), Energetic ion acceleration in Saturn's magnetotail: Substorms at Saturn? *Geophys. Res. Lett.*, *32*, L20S01, doi:10.1029/2005GL022647.

Mitchell, D. G., P. C. Brandt, E. C. Roelof, J. Dandouras, S. M. Krimigis, and B. H. Mauk (2005b), Energetic neutral atom emissions from Titan interaction with Saturn's magnetosphere, *Science*, *308*(5724), 989–992, doi:10.1126/science.1109805.

Pollock, C. J., et al. (2000), Medium Energy Neutral Atom (MENA) imager for the IMAGE mission, *Space Sci. Rev.*, *91*, 113–154, doi:10.1023/A:1005259324933.

Williams, D. J., E. C. Roelof, and D. G. Mitchell (1992), Global magnetospheric imaging, *Rev. Geophys.*, *30*, 183–208, doi:10.1029/92RG00732.